ADVANCED OPTICAL MATERIALS
www.advopticalmat.de

Remarkable Plasmonic Enhanced Luminescence of Ce^{3+}doped Lanthanide Downconversion Nanoparticles in NIR-II Window by Silver Hole-Cap Nanoarrays

*Jiamin Xu, Ming Fu, Yao Lu, Anthony Centeno, Jingdong Xu, Xiaofei Xiao, Qiyu Zhang, Koen Evers, Yunfan Xu, Rico Lim, Changxu Liu, Stefan A Maier, Rupert Oulton, Mary P Ryan, and Fang Xie**

Lanthanide downconversion nanoparticles (DCNPs) have huge potential in biosensing and imaging applications in the NIR-II window. However, DCNPs inherently suffer from low quantum efficiency, due to low absorption cross-section and the restricted doping concentration of lanthanide ions. In this work, a combined strategy for downconversion luminescence in the NIR-II window is investigated by the integration of Ce^{3+} ions into the conventional $NaYF_4$: Yb^{3+}, Er^{3+} DCNPs and incorporation of periodic silver hole-cap coupled Nanoarrays (Ag-HCNAs) simultaneously. Over two orders of magnitude, luminescence enhancement is achieved by the combination of optimized Ce^{3+} doping and plasmonic effects, compared to $NaYF_4$: Yb^{3+}, Er^{3+} DCNPs immobilized on the glass substrate. Moreover, 3D Finite-Difference Time-Domain (FDTD) simulations and time-resolved luminescence measurements are combined to gain important insights into the mechanism of downconversion luminescence enhancement. The results show that there is a large electric field enhancement between the Ag nanoholes and the Ag hemisphere cap at 980 nm (excitation enhancement), while the lifetime shortening at 1525 nm revealed an increased radiative decay rate and enhanced quantum yield (emission rate enhancement). The strategy for downconversion luminescence enhancement demonstrated in this work holds a significant potential for advancing the next generation biosensing and bioimaging based on DCNPs in the NIR-II window.

1. Introduction

Lanthanide-doped downconversion nanoparticles (DCNPs) are currently at the forefront of research, especially in the field of molecular sensing, biomedical imaging, and theranostics, owing to their remarkable luminescent properties within the second near-infrared (NIR-II, 1000–1700 nm) biological window.[1–8] Luminescence within the NIR-II region offers numerous advantages, including reduced scattering, reduced absorption, lower phototoxicity, and minimal autofluorescence originating from biological tissues and/or media, which empowers the generation of bright fluorescent signal through deep-tissue in a minimal invasive approach. The NIR-II fluorescent signal transcends the limitations of visible (380–700 nm) and NIR-I regions (780–1000 nm), allowing for high spatial resolution imaging or detection sensitivity both in vivo and ex vivo.[9–11] On the other hand, DCNPs exhibit a large Stokes shift accompanied by sharp

J. Xu, Y. Lu, Q. Zhang, K. Evers
Department of Materials
Imperial College London
Exhibition Road, London SW7 2AZ, United Kingdom
M. Fu, X. Xiao, Y. Xu, R. Lim
Department of Physics
Imperial College London
Exhibition Road, London Sw7 2AZ, United Kingdom

The ORCID identification number(s) for the author(s) of this article can be found under https://doi.org/10.1002/adom.202400660

DOI: 10.1002/adom.202400660

A. Centeno
James Watt School Of Engineering
University of Glasgow
James Watt South Building, Glasgow, Scotland G12 8QQ,
United Kingdom
J. Xu
Imperial College London
Exhibition Road, London SW7 2AZ, United Kingdom
C. Liu, R. Oulton, M. P Ryan
University of Exeter
Stocker Rd, Exeter EX4 4PY, United Kingdom
S. A Maier
Monash University
Wellington Road, Clayton, Melbourne, Victoria 3800, Australia
F. Xie
Department of Materials
Imperial College London
Prince Consort Road, London SW7 2AZ, United Kingdom
E-mail: f.xie@imperial.ac.uk

emission bands, which enables the efficient separation of excitation and emission wavelengths. Consequently, the signal-to-noise ratio could be dramatically improved.

Typically, DCNPs consist of a low-phonon energy host lattice and a combination of sensitizer and activator lanthanide ions. By selecting different lanthanide types, a range of sensitizer-activator pairs can be formed, allowing control over energy transfer processes and the resulting absorption and emission features across the visible NIR-II regions. However, practical applications of NIR-II emitting DCNPs are hindered by their inherent low quantum yields. This limitation is primarily attributed to the partially forbidden *4f-4f* electronic transitions of lanthanide ions within a host lattice, leading to a narrow band of absorption.[12,13] Furthermore, energy transfer pathways between sensitizer-activator pairs give rise to two categories of luminescence: upconversion luminescence (UCL) and downconversion luminescence (DCL).[14–16] Regarding the use of DCNPs in biological *applications* in vivo or in vitro, NIR-II DCL should dominate over the other forms of luminescence. However, the presence of UCL in the visible region and DCL in the NIR-II window results in competition within DCNPs, further reducing the efficiency of NIR-II emission. Despite this, researchers have found a viable approach to enhance the population of electrons into a specific energy state, thereby contributing to NIR-II DCL, while suppressing the UCL processes. Zhai et al. reported that the introduction of 2% Ce^{3+} ions into cubic-phase $NaYF_4$:20%Yb^{3+},2%Er^{3+} resulted in an enhancement of emission at 1525 nm, albeit at the expense of suppressing all other UCL emissions.[17] A similar outcome was also observed by Zhong et al., who reported that the incorporation of 2% Ce^{3+} ions in $NaYbF_4$: 2%Er^{3+} nanoparticles resulted in increased 1550 nm emission by up to 9-fold.[18] Plasmonic modulation provides an alternative novel approach to amplify emitting photons from luminescent probes, such as dyes,[19,20] quantum dots,[21–23] and upconversion nanoparticles,[24–26] by coupling them with plasmonic nanostructures. The resulting fluorescence enhancement can be attributed to two main factors. First, excitation enhancement, occurs when the fluorophores experience a strong localized electric field across the surface of the plasmonic antenna, thereby accelerating the excitation rate.[27,28] Second, emission enhancement, which arises from an acceleration of radiative decay rate when the LSPR of an antenna closely matches the emission band of the luminescent probes, leads to a decrease in their lifetime and an increase in quantum yield.[29–31]

The utilization of a plasmonic platform to amplify NIR-II DCL from DCNPs is relatively scarce.[32] In the domain of biosensing applications, especially in the context of metal-enhanced fluorescence (MEF) based immunoassays,[32] fluorescent probes must form a resilient attachment onto the plasmonic substrate. This attachment is facilitated by a self-assembled monolayer (SAM) of molecular spacers, ensuring stability even after undergoing multiple rounds of washing steps.[33–35] Earlier investigations into fluorescence immunoassays have revealed a significant limitation in the Limit of Detection (LOD) of traditional dyes like Rhodamine, Fluorescein isothiocyanate, or cyanine. This limitation stems from adverse background signals induced by fluctuations in light intensity, autofluorescence, sample complexity, and electronic features throughout the measurement process.[36] These optical noises limit detection sensitivity and introduce experimental errors. In contrast, the adoption of NIR-II emissive immunoassay platforms can mitigate these unwelcome background noises and improve the sensitivity and accuracy of detection targets.[37–39] Therefore, a systematic exploration that incorporates the application of a monolayer of DCNPs onto a plasmonic substrate holds substantial promise. This approach not only enables the optimization of the enhancement factor by manipulating the plasmonic effect but also paves the way for potential advancements in MEF-based immunoassay research using NIR-II emitting DCNPs.

In this work, we successfully immobilized a sub-monolayer of polyacrylic acid (PAA) functionalized DCNPs. This was achieved through a robust amide bond to conjugate them with the bifunctional thiol-PEG-amine polymeric dielectric layer pre-grafted onto the Ag hole-cap coupled nanoarrays (Ag-HCNA). 3D Ag-HCNA with finely controlled extinction features were fabricated using a simple yet robust colloidal lithography method,[30] illustrated in **Scheme 1**. Initially, the PS spheres' self-assembled film was shrunk to enable the deposition of a metallic layer on the glass gaps between adjacent PS spheres, as well as on the upper hemispheres of PS spheres. Furthermore, we systematically investigated a combined effect of Ce^{3+} dopants and plasmonic modulation to increase the NIR-II emission of DCNPs. To achieve this, two types of DCNPs, $NaYF_4$:20%Yb^{3+}, 2%Er^{3+}, 10%Ce^{3+}, and $NaYF_4$:20%Yb^{3+}, 2%Er^{3+}, were deposited onto the Ag-HCNA film. When excited at 980 nm, a remarkable 25-fold enhancement was observed at 1525 nm, corresponding to Er^{3+} emission, in Ce^{3+} doped DCNPs, coupled with Ag-HCNA, exhibiting an optimal spectral overlap.

2. Experimental Section

2.1. Chemicals and Materials

Sodium hydroxide (NaOH, ≥98%), Erbium(III) acetate hydrate (99.9%), Ytterbium(III) acetate tetrahydrate (99.9%), Yttrium(III) acetate hydrate (99.9%), Cerium(III) acetate hydrate (99.9%), Gadolinium(III) acetate hydrate (99.9%), Neodymium(III) acetate hydrate (99.9%), Ammonium fluoride (NH_4F, 96%), Cyclohexane (99.5%), Oleic acid (OA, 90%), and 1-Octadecene (ODE, 90%), Poly(acrylic acid) (PAA), methanol (≥99.9%), Silicon wafers, and Sodium dodecyl sulfate (SDS, >99.0%), phosphate buffered saline (PBS), 2-(N-morpholino)ethanesulfonic acid hydrate (MES), 1-ethyl-3-(3-dimethylaminopropyl)carbodiimide hydrochloride (EDC), n-hydroxysuccinimide (NHS), were purchased from Sigma–Aldrich. Thiol-PEG-Amine, HCl salt (SH-PEG7500-NH_2, MW: 7500) was bought from JenKem Technology, Texas, USA. Monodisperse Polystyrene solution (5% w/v, 617 nm) was purchased from Bangs Laboratories. All chemicals were used without further purification.

2.2. Synthesis of NaYF4: 20%Yb^{3+}/2%Er^{3+}/X%Ce^{3+} DCNPs (X = 0, 2, 4, 6, 10, 15)

Following a typical solvent-thermal method,[40] a total of 1 mmol of Erbium (III) acetate hydrate, Ytterbium (III) acetate tetrahydrate, Yttrium (III) acetate hydrate, and Cerium (III) acetate hydrate powders were mixed in a three-neck round bottom flask,

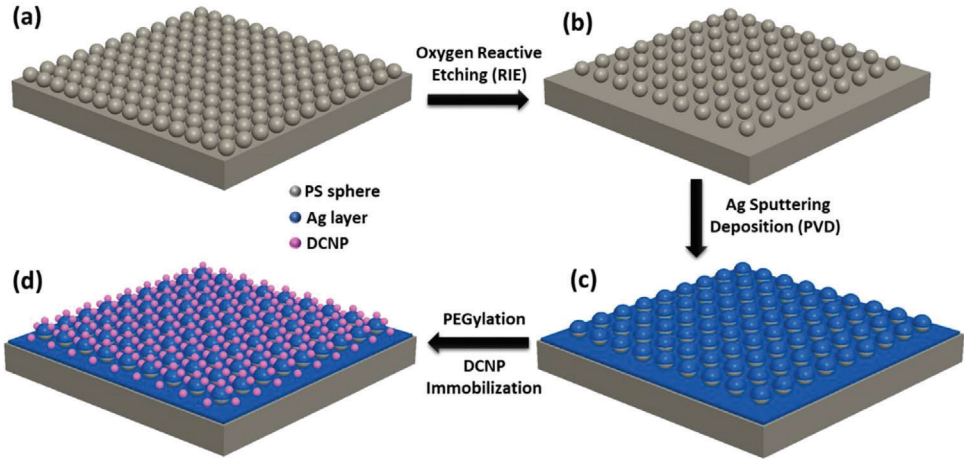

Scheme 1. Schematic illustration of the workflow of MEF on Ag-HCNA films: a) A monolayer of closely packed PS spheres on a glass slide, b) Formation of hexagonally ordered shrunk PS spheres through RIE, c) Formation of Ag-HCNA film through Ag sputtering, d) Immobilizing a sub-monolayer of DCNPs onto Ag-HCNA film.

using a molar ratio (Yb: Y: Er: Ce) of 20: 78-X: 2: X. To this mixture, 7.5 mL of OA and 15 mL of ODE were then added with vigorous stirring. The mixture solution was heated to 145 °C and maintained at that temperature for 1 h under vacuum until a transparent faint-yellow solution was obtained. After cooling the solution to 50 °C, a mixture of 4 mmol of NH_4F and 2.5 mmol of NaOH was dissolved in 10 mL of methanol. The resulting turbid solution was stirred vigorously at a temperature below 50 °C for 30 min, followed by heating up to 110 °C under vacuum to remove excessive water and methanol. Once no bubbles were observed, the orange solution was heated to 298 °C under an argon atmosphere and maintained at that temperature for 90 min. After completion of the reaction, the solution was cooled to room temperature and subsequently centrifuged at 5000 rpm for 15 min. The resulting pellet was finally redispersed in cyclohexane.

2.3. Preparation of Ligand-Free DCNPs

A mild HCl treatment was employed to eliminate the attached oleate ligands from the surface of DCNPs.[41] Briefly, the pellet DCNPs obtained after centrifuge were re-dispersed in 15 mL ethanol. A few drops of diluted HCl (0.1 M) were added until the PH value of the solution was 4. The acidic solution was sonicated for 30 min and then stirred overnight at room temperature. The resulting ligand-free nanoparticles were washed with ethanol and water and were finally dispersed in water.

2.4. Preparation of PAA Modified DCNPs (PAA-DCNPs)

As previously reported,[42] 0.2 g of PAA powder was mixed with ligand-free DCNPs in 10 mL of water. The mixture was vigorously stirred, and a few drops of 1 M NaOH solution were slowly added until the pH of the solution reached 8. The stirring was continued for 24 h at room temperature. The obtained nanoparticles were collected by centrifugation at 10 000 rpm for 15 min, washed multiple times with ethanol and water, and then redispersed in 10 mL of water. Finally, the nanoparticles were stored in a refrigerator at 4 °C until used.

2.5. Fabrication of Silver Hole-Cap Coupled Nanoarray (Ag-HCNA)

Initially, A monolayer of PS spheres was coated onto glass slides via a previously reported self-assembly technique.[30,43] Briefly, the commercially available polystyrene sphere solution (PS617) was 1:1 diluted with ethanol, followed by 15 min of ultrasonication. Simultaneously, glass slides (10 mm × 10 mm) and silicon wafers (150 mm in diameter) were cleaned sequentially with acetone, ethanol, and ultrapure water, each for 5 min using ultrasonication, followed by drying with nitrogen. These cleaned glass slides and wafers were then treated with UV-ozone for 1 h. Thereafter, an aliquot of diluted PS solution was dropwise deposited onto the silicon wafer. After spreading and drying the PS beads, the wafer was gradually immersed into a glass vessel filled with 200 mL of DI-water supplemented with several drops of 2% SDS solution. As a result, a monolayer assembly was detached from the silicon wafer and floated in the water. Finally, The PS bead monolayer assembly was transferred from water onto glass slides and dried under a fume hood for 24 h.

The fabrication of Silver Hole-Cap Nanoarrays film (Ag-HCNA) involved a modified colloidal lithography method.[43] The monolayer of PS spheres obtained on the glass slide was treated by reactive ion etching (RIE) using O_2 for 50 and 60 s, with an O_2 pressure of 20 Pa, O_2 flow rate of 20 sccm, and RF power of 100 W to fabricate Ag-HCNA (50) and Ag-HCNA (60) films, respectively. Afterward, a 50 nm thick layer of Ag was sputtered onto the etched PS sphere substrate using a Hex deposition system, with an argon flow rate of 10 sccm, a voltage of 630 V, and a current of 100 mA. The deposition thickness of the Ag layer was monitored by a quartz crystal monitor (QCM) integrated into the sputtering system. The as-obtained substrate sample was heated onto a hot plate at 90 °C for 2 min and stored in a desiccator covered with aluminum foil before use.

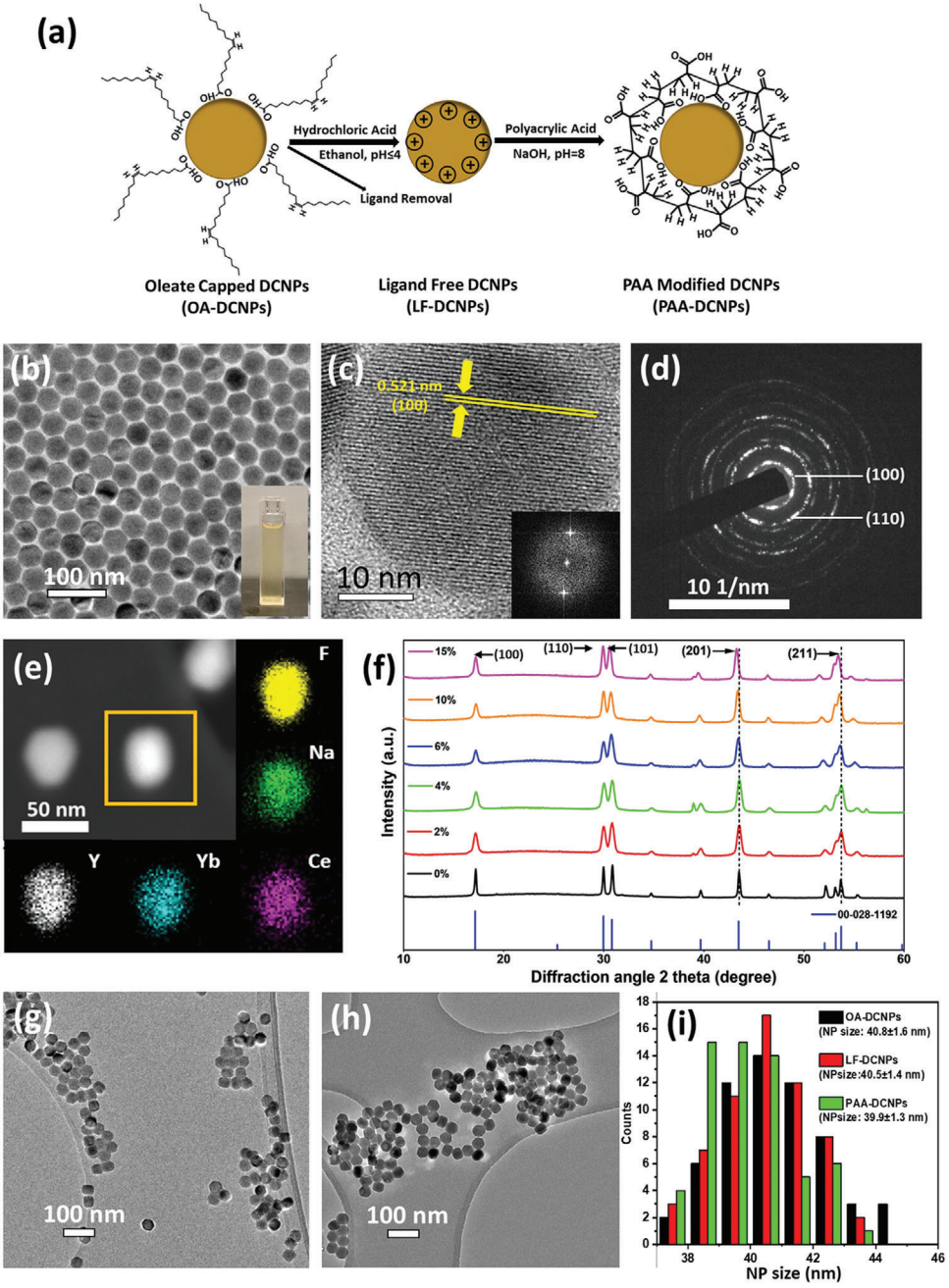

Figure 1. Morphological features of NaYF4: 20%Yb^{3+}, 2%Er^{3+},10%Ce^{3+} DCNPs. a) Scheme of ligand exchange reaction to produce PAA-DCNPs. b,g,h) TEM images of (a) Oleate capped (OA-DCNPs), f) Ligand free (LF-DCNPs), g) PAA functionalized DCNPs (PAA-DCNPs), respectively. c) High-magnitude TEM image of single DCNP, inset: the corresponding FFT pattern. d) SAED image corresponding to (b). e) Elemental mapping of single DCNP from STEM-EDX mode. f) XRD patterns of $NaYF_4$: 20%Yb^{3+}, 2%Er^{3+}, X%Ce^{3+} DCNPs with different Ce^{3+} doping concentrations, where X = 0, 2, 4, 6, 10, and 15, respectively. The blue vertical lines show the reference stick Pattern of hexagonal $NaYF_4$: 39%Yb^{3+}, 4%Er^{3+} crystalline structure, indexed by 00-028-1192. i) Size distribution histograms of OA-DCNPs, LF-DCNPs, and PAA-DCNPs.

2.6. Immobilization of a Sub-Monolayer of PAA-DCNPs onto Ag-HCNA

The immobilization of DCNPs onto Ag-HCNA was accomplished using an NHS-EDC conjugation method.[21,44] Briefly, 50 mg of SH-PEG7500-NH_2 powder was dissolved in 1 mL of ethanol and sonicated for 30 min. Later, 50 µl of the SH-PEG7500-NH_2 solution was deposited onto Ag-HCNA, and the sample was incubated in a sealed petri dish for 30 min. Excess SH-PEG7500-NH_2 was then removed by rinsing with water and ethanol. To activate the carboxyl groups on the surface of PAA-DCNPs, 55 µl of PAA-DCNPs solution (1 mg mL^{-1}) was mixed with 80 µl of 10 mM EDC and 80 µl of 25 mM NHS for 15 min. Then, 1.1 mL of PBS solution was added, and 20 µl of the now-activated

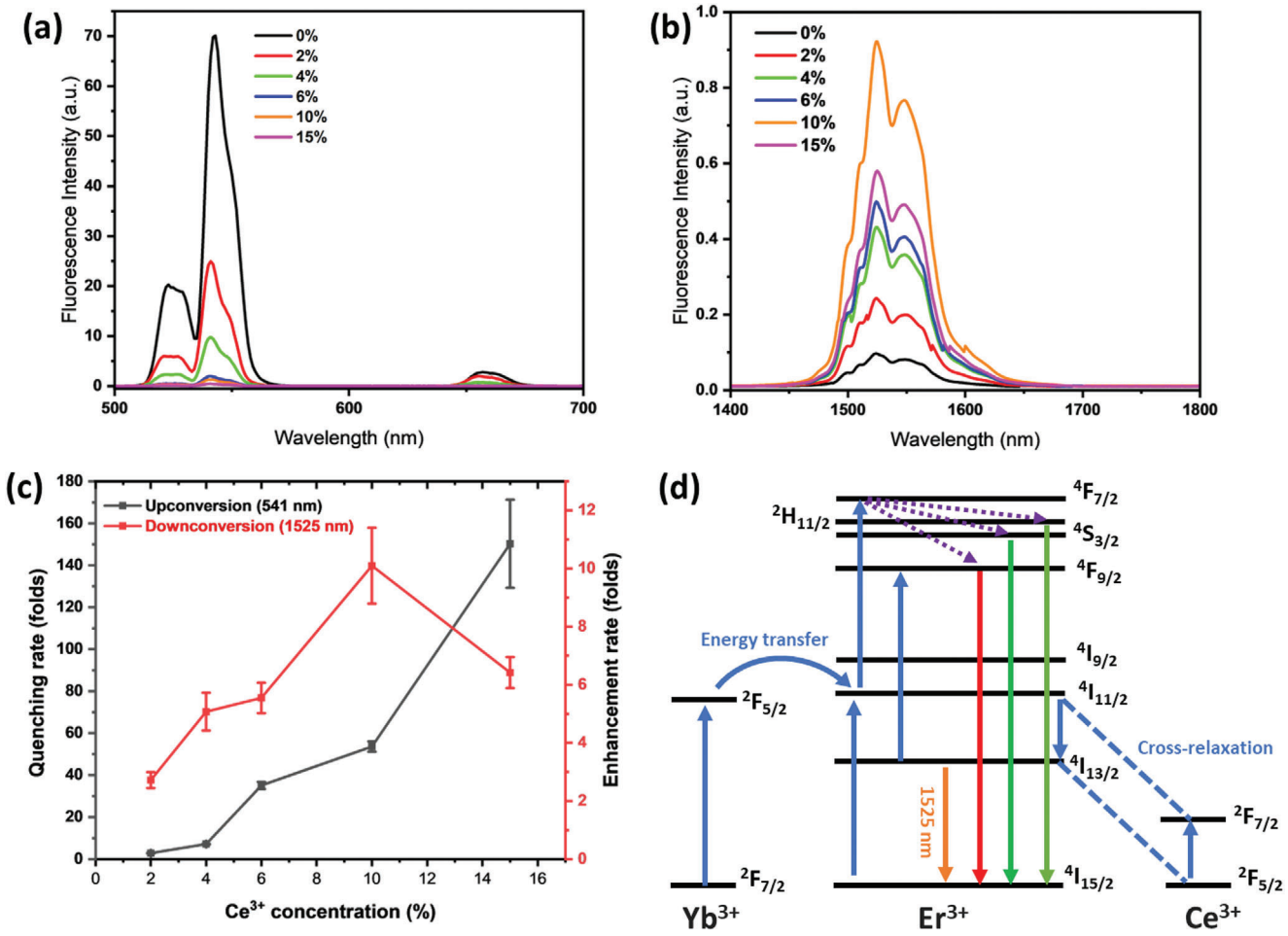

Figure 2. Photoluminescence (PL) properties of OA-DCNPs (a,b) PL spectra of cyclohexane dispersed $NaYF_4$: 20%Yb^{3+}, 2%Er^{3+}, X%Ce^{3+} DCNPs with different concentrations of Ce^{3+} (X = 0, 2, 4, 6, 10, 15) across a) visible and b) NIR-II regions under the irradiation of a CW-980 nm (0.8 W) laser. c) Quenching rate (black curve) and enhancement rate (red curve) of visible UCL and NIR-II DCL as a function of Ce^{3+} doping concentrations. (d) Simplified energy-level diagrams illustrating the possible energy transfer pathways between Yb^{3+}, Er^{3+}, and Ce^{3+}. The solid upper arrow, solid down arrow, and dashed down arrow represent the excitation, radiative, and non-radiative decay processes, respectively.

nanoparticle solution was deposited onto the PEGylated Ag-HCNA. The sample was incubated in a sealed peri dish for 3 h, and the unbound nanoparticles were then rinsed off and collected. With the known fluorescence intensity of the total amount of DCNPs and unbound DCNPs, the amount of DCNPs can be determined. As a reference, a clean glass slide was functionalized with APTES using a previously reported method and then equally immobilized with DCNPs using the same conjugation method. Each film sample bound with DCNPs was then dried with nitrogen and stored in a desiccator covered with aluminum foil before measurement. According to the previously reported protocols,[20,31] fluorescence enhancement was assessed by comparing the emission intensity of DCNPs immobilized on each type of Ag-HCNA film with DCNPs on the glass as a control. The average fluorescence enhancement was obtained based on $Enh_{total} = (I_{Ag}/I_{glass})(N_{glass}/N_{Ag})$, where I_{Ag}, and I_{glass} denote the DCL intensity from DCNPs immobilized on Ag-HCNA and glass, respectively. N_{Ag} and N_{glass} represent the amount of DCNPs bound onto Ag-HCNA and glass, respectively. The average enhancement factors and standard deviations were determined by averaging measurements from nine distinct regions of each array sample.

2.7. Characterization

X-ray diffraction (XRD) patterns of DCNPs were obtained using a PANalytical MPD. The X-ray source was Cu Kα irradiation (k = 1.5406 Å), and the measurement range (2θ) spanned from 10° to 70° with a step size of 0.0167°. The morphologies of DCNPs were characterized using JEOL2100 plus Transmission electron microscope (TEM), equipped with energy-dispersive x-ray spectroscopy (EDX, Oxford Instruments, UK), at an accelerating voltage of 200 kV. TEM samples were prepared by drop-casting onto a copper grid coated with a carbon film and naturally dried before use. The morphologies of substrate samples were characterized by a LEO Gemini 1525 Field Emission Gun Scanning electron microscope (SEM) using an InLens detector, at an acceleration voltage of 5 kV. The equipped Energy-dispersive X-ray spectroscopy (EDX, from Oxford Instruments,

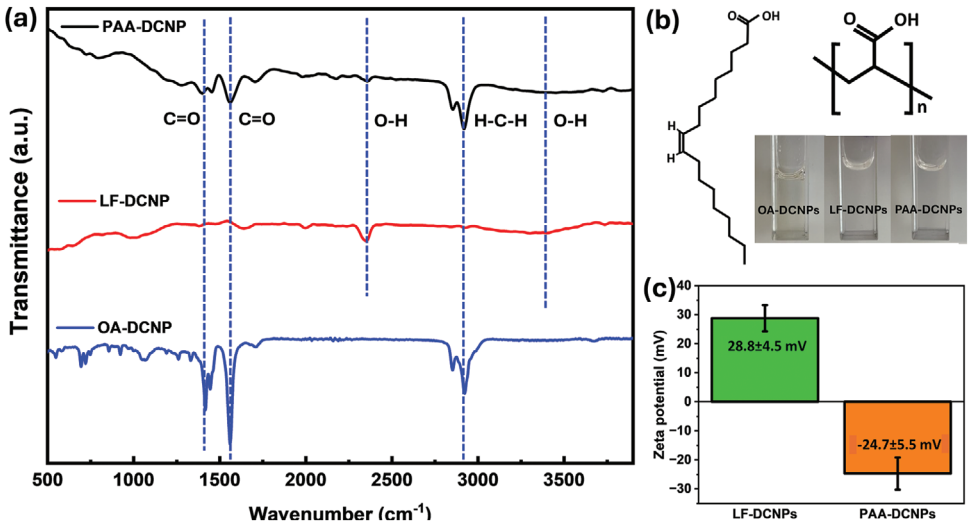

Figure 3. Surface functionalization of DCNPs a) FTIR spectra of DCNPs functionalized with different types of surface ligands. b) Schemes of molecular formula of OA (left) and PAA (right), inset digital camera images of cyclohexane dispersed OA-DCNPs (left), aqueous LF-DCNPs (middle) and aqueous PAA-DCNPs (right). c) Zeta potential of LF-DCNP and PAA-DCNPs dispersed in aqueous solution.

UK) mode was performed at 20 kV. The extinction spectrum of both substrate and solution samples was characterized using a UV–vis–NIR spectrophotometer (Agilent Cary 5000). The solution sample was loaded into a high-performance quartz cuvette and the measurement ranged from 800 to 1200 nm. The substrate sample was measured from 400 to 1600 nm. Fourier transform infrared (FTIR) spectra were recorded using a Bruker Vector 22 FTIR spectrometer equipped with a DGTS detector, while the contact angle was measured by the Attension Theta (Biolin Scientific). The surface charge of DCNPs with different grafting conditions was characterized by a zeta potential analyzer (Nano ZS ZEN3600, Malvern). The aqueous nanoparticles solution was loaded in a DTS1070 capillary cell with a neutral pH value.

Fluorescence spectra of solution-phase DCNPs loaded into a quartz cuvette were measured by a Fluorolog Tau3 system (Horiba Scientific) connected to an MDL–980 nm continuous-wave (CW) laser (Changchun New Industries Optoelectronics Technology Co., Ltd.). The visible emission spectra (500–900 nm) were collected by using a self-contained Photon Counting PMT Detection System, and the NIR-II (1300–1700 nm) emission spectra were collected by using a 512 element TE-cooled InGaAs array near-IR detector. The NIR-II emission spectra of substrate samples were measured by a nitrogen cooled (−120 °C) InGaAs camera spectrometer (Princeton Instruments Spec 10 system with an SP2300) equipped with A CW laser diode at a wavelength of 980 nm. The visible upconversion lifetime profiles of DCNPs doped with various concentrations of Ce^{3+} ions were characterized using a time-correlated single-photon counting (TCSPC) technique provided by Horiba Scientific. Building upon the previous report,[45] the powder-formed nanoparticle samples were excited by a pulsed laser with a peak wavelength of 976 ± 10 nm, an average power of 0.2 mW, and a repetition rate of 50 MHz. The lifetimes of 0% and 10% Ce^{3+} doped PAA-DCNPs, when placed on glass and Ag-HCNAs, were characterized using a frequency domain lifetime measurement technique with modulated pump and detection methodology, previously established in the prior work.[43,46]

2.8. Numerical Modelling

The simulated extinction and local electric field (E-field) mapping was conducted on two types of Ag hole-cap nanoarrays (Ag-HCNA) using the open-source Finite Difference Time Domain (FDTD) software MEEP.[47] The model featured a hexagonal arrangement of PS spheres on a glass substrate, as previously outlined in the prior work.[43] In the model, the sphere diameter for Ag-HCNA(50) and Au-HCNA(60) were 422 and 340 nm respectively. A 50 nm thick layer of Ag was deposited on the upper surface of both the glass and PS spheres. A visual representation of this geometry is shown in Scheme 1 and Figure S6 (Supporting Information). In this FDTD model, the Ag was characterized using a Drude–Lorentz model, while the PS spheres and the glass substrate had a refractive index of 1.54 and 1.52, respectively.[43,48] Perfectly matched layers (PMLs) were used at the upper and lower boundaries of the computational domain to minimize non-physical reflections. Periodic boundaries were implemented in two other dimensions to simulate an infinite hexagonal array of PS nanospheres with nano-cap arrays. The FDTD cell resolution was set to 5 nm in each direction, which was determined by convergence testing. The computational simulations were run using the ARCHIE–WEST High-Performance Computer (www.archie-west.ac.uk). The reflections, absorption, and transmission of nanoarrays were calculated using a method described previously,[49] where the incident, transmitted, and backscattered fields are found through computational surfaces placed in the glass and above the nanoarray. The nanoarray was excited using an incident plane wave normal to the upper surface.

Purcell factor simulations were conducted using the commercial FDTD software Lumerical. 3D simulations were

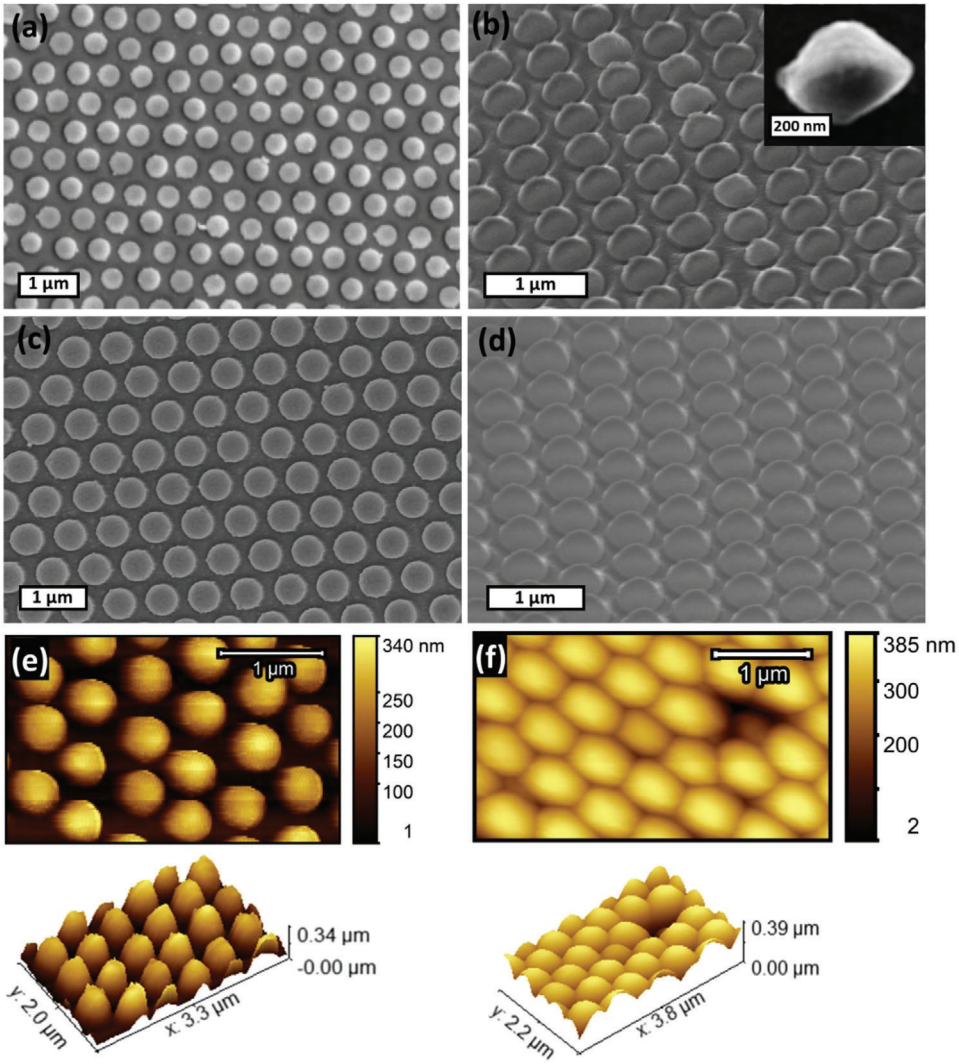

Figure 4. Morphologies of Ag-HCNA films a–d) SEM images of a,b) Ag-HCNA(60) and c,d) Ag-HCNA(50) films in a,c) a vertical view, and b,d) a 60° tilted view, inset b): a cross-sectional view of an isolated Ag hemisphere cap. e,f) AFM topology image and the respective 3D profile of (e) Ag-HCNA(60) and (f) Ag-HCNA(50) films.

implemented with the PML boundaries applied to the upper and the lower boundaries, and the periodic boundaries were applied to the other 2D. The emitter was modeled as an electric dipole. An overwrite mesh region with a uniform mesh size of 4 nm (to balance the simulation time and accuracy) fully enclosed the dipole and the silver structures. Three dipoles with different orientations (aligned to the x, y, and z-axis) were simulated in three simulation files at each point. The average Purcell factor was calculated by averaging these Purcell factors for these three orientations. To simplify the simulation, all points were confined to the xOz plane. The simulated configuration, as illustrated in Figure 8e, featured dipoles positioned at four selected locations denoted as A to D, with a consistent perpendicular distance of 30 nm from each dipole to the Ag-HCNA surface. Specifically, Points A and D were aligned with the X-axis and Z-axis, respectively. Point A sat on the plane of z = 50 nm, while Point D was situated on the x = 0 nm plane.

3. Results and Discussion

Figure 1a depicts the proposed ligand exchange mechanism, associated with the removal of oleate ligands under an acidic solution and the subsequent new ligand grafting process under an alkaline condition. A solvent-thermal method in an OA/ODE system was employed for the synthesis of oleate-capped NaYF4: 20%Yb^{3+},2%Er^{3+},10%Ce^{3+} DCNPs (OA-DCNPs), with an average size of 40 nm (Figure 1b). The *d-spacing* of ≈0.521 nm (Figure 1c) corresponds to the (100) plane of the hexagonal phase of $NaYF_4$, which is in agreement with the observed Selected Area Electron Diffraction (SAED) pattern in Figure 1d and the corresponding XRD pattern (orange) in Figure 1f. Elemental mapping (Figure 1e) and the corresponding EDX spectrum (Figure S1, Supporting Information) confirmed the major chemical compositions of the resultant nanoparticles contained Na, Y, F, Yb, and Ce. Due to the abundant hydrophilic carboxyl

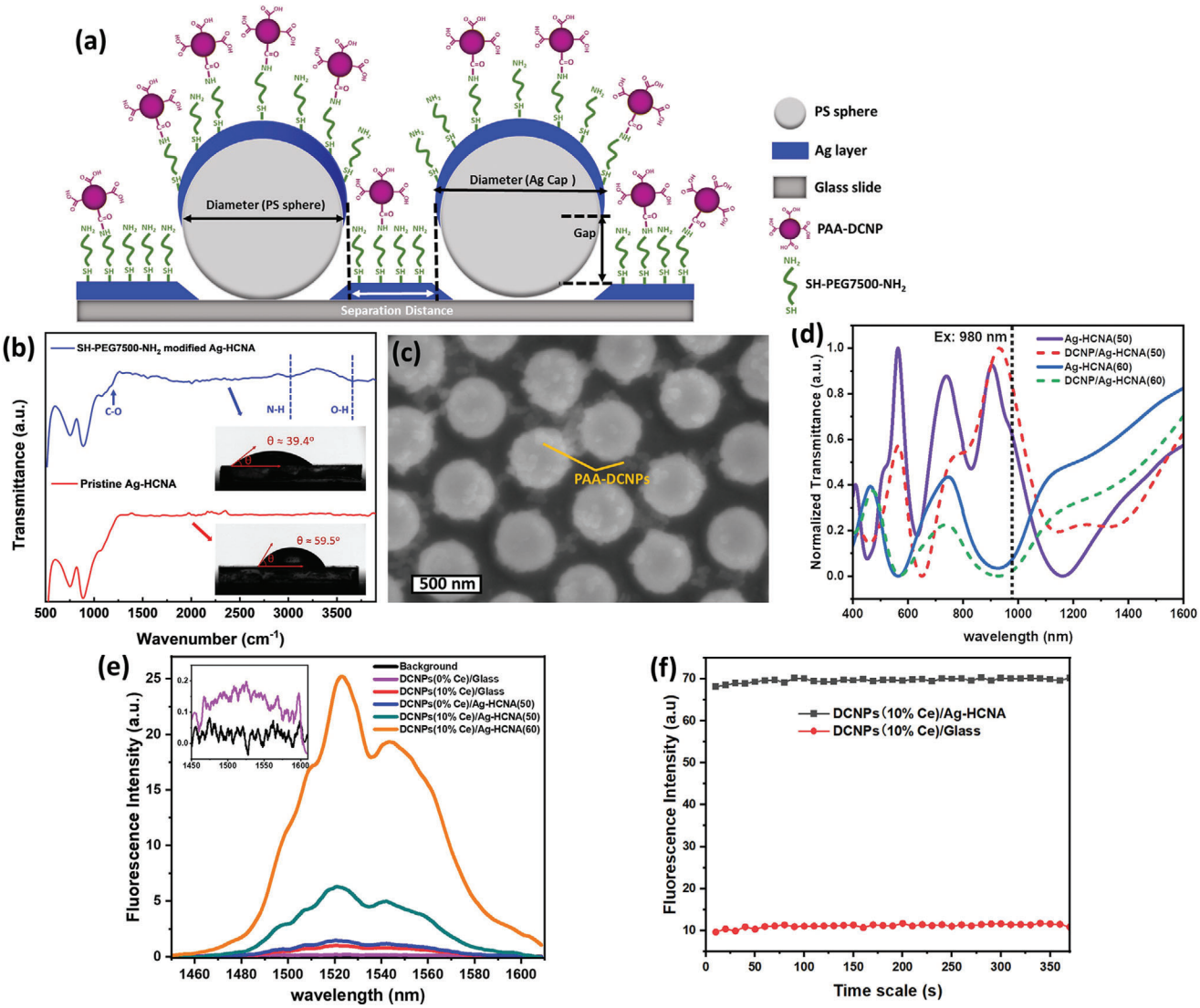

Figure 5. Immobilization of a sub-monolayer of DCNPs onto Ag-HCNA and the related NIR-II DCL enhancement study. a) scheme of crosslinker Chemistry between PAA-DCNPs and PEGylated Ag-HCNA. b) FTIR spectra of Ag-HCNA film before and after PEGylation, insets the measured contact angles of respective films. c) SEM image of a sub-monolayer of PSS-DCNPs immobilized on PEGylated Ag-HCNA(50). d) Extinction spectra of pristine Ag-HCNA, PAA-DCNPs immobilized on PEGylated Ag-HCNA (DCNPs/Ag-HCNA), and the black dotted line shows the absorption position of sensitizer Yb^{3+} ions within DCNPs. e) PL spectra of a sub-monolayer of PSS-DCNPs doped with 10% or 0% of Ce^{3+} on a glass slide and Ag-HCNA films. f) Fluorescence stability test.

groups from PAA, this functionalization process is proposed to significantly improve the aqueous stability and biocompatibility of nanoparticles. The morphologies of aqueously dispersed ligand-free (LF-DCNPs) and PAA functionalized DCNPs (PAA-DCNPs) are shown in Figure 1g,h. The shape and size of the DCNPs remained unchanged following the ligand exchange process (Figure 1i).

Upon doping the $NaYF_4$ host matrix with different concentrations of Ce^{3+} ions ranging from 0% to 15%, the shape and uniformity of the resultant nanoparticles showed negligible differences (Figure S2, Supporting Information). XRD patterns (Figure 1f) shows that the characteristic peaks of all measured samples can be perfectly indexed to β-$NaYF_4$ (JCPDS card No. 00-028-1192), indicating no other impurity phases. This implied the complete consumption of NaOH and NH_4F during the stages of $NaYF_4$ nucleation and growth. With increasing Ce^{3+} ion concentration from 0% to 15%, the obvious blueshifts at peaks corresponding to the (201) and (211) planes were attributed to lattice expansion. The incorporated Ce^{3+} ions substituted Y^{3+} ions in the original $NaYF_4$ lattice and led to lattice expansion due to the larger ionic radius of the Ce^{3+} ion (≈0.101 nm) compared to the Y^{3+} ion (≈0.09 nm). Consequently, the nanoparticles doped with Ce^{3+} ions showed a larger size compared to the Ce^{3+} ion free counterpart (Figure S3, Supporting Information).

Under a 980 nm laser irradiation, the cyclohexane dispersed OA-DCNPs exhibited multiple emission bands from the visible to NIR-II regions (**Figure** 2a,b). The emission peaks of 525, 541, and 665 nm were ascribed to the "two-photon" upconversion

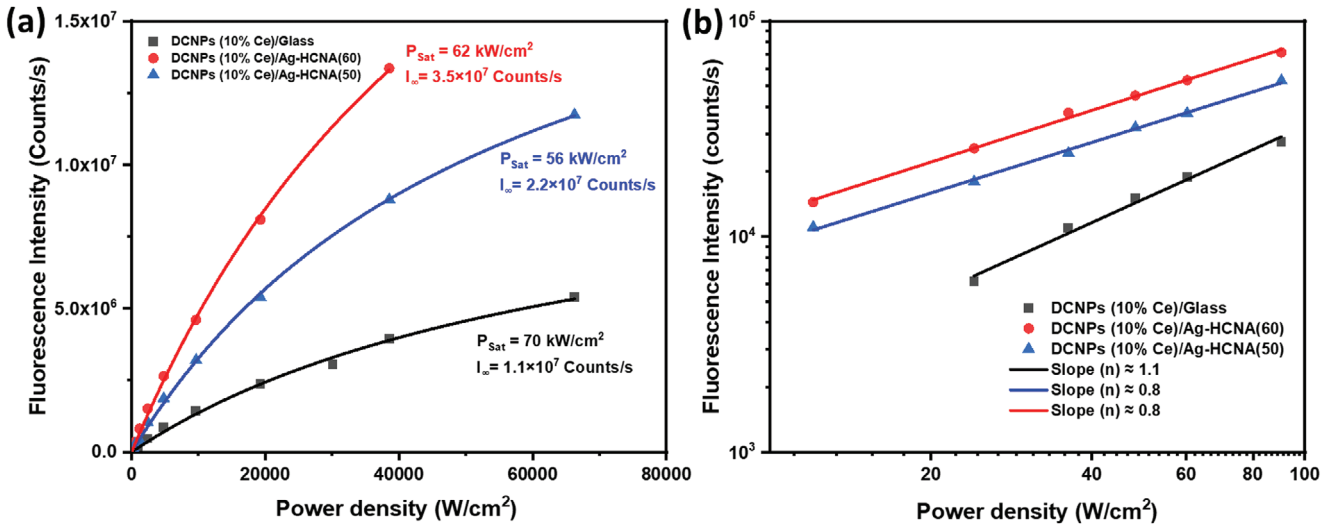

Figure 6. Photophysical properties of Er^{3+} induced NIR-II DCL photons from DCNPs on glass and Ag-HCNAs a) Fluorescence saturation curves show a maximum emission rate of 1.1×10^7 Counts s^{-1} for DCNPs (10% Ce) on glass and 2.2×10^7 Counts s^{-1} for DCNPs (10% Ce) on Ag-HCNA(50) and b) Log-log plot of Power density versus fluorescence intensity of both samples at a low excitation regime.

luminescence (UCL) decays, whereas the NIR-II emission peak at 1525 nm followed the conventional "one-photon" downconversion luminescence (DCL) process.[26,50] With increasing Ce^{3+} ion concentration from 0% to 10%, the emission intensity of NIR-II DCL was significantly boosted at the cost of UCL quenching. It was found that 10% was the optimum doping concentration for the brightest NIR-II emission at 1525 nm, which was ≈10-fold brighter than that from 0% doped DCNPs (Figure 2c). Further increasing the Ce^{3+} ion concentration from 10% to 15% led to quenching. The proposed energy-transfer diagram in Figure 2d illustrates a cascade of energy transfer and decay pathways that might occur when the DCNPs are excited at 980 nm. The initially populated $^2F_{5/2}$ (Yb^{3+}) states transferred energy to the adjacent $^4I_{11/2}$ (Er^{3+}) states. The small energy mismatch between the $^2F_{5/2}$ (Yb^{3+}) state and $^4I_{11/2}$ (Er^{3+}) was made up for by the vibronic coupling effect between dopant ions and the surrounding lattice phonons, allowing the occurrence of phonon-assisted energy transfer process between two neighboring lanthanide ions. Due to the long-lived intermediated states within Er^{3+}, the populated electrons in the $^4I_{11/2}$ (Er^{3+}) states can be further excited to the $^4F_{9/2}$ (Er^{3+}) and $^4F_{7/4}$ (Er^{3+}) states. After a series of non-radiative relaxation processes, the filled electrons on the $^2H_{11/2}$ (Er^{3+}), $^4S_{3/2}$ (Er^{3+}) $^4F_{9/2}$ (Er^{3+}) states radiatively decay to the $^4I_{15/2}$ (Er^{3+}) state, emitting visible UCL photons at 525, 541, and 665 nm, respectively. Additionally, a portion of electrons on the $^4I_{11/2}$ (Er^{3+}) states non-radiatively decayed to $^4I_{13/2}$ (Er^{3+}) states, emitting NIR-II DCL photons at 1525 nm through the $^4I_{13/2}$ (Er^{3+}) to $^4I_{15/2}$ (Er^{3+}) transition. Since UC in the visible region and DC in the NIR-II window were two competitive luminescence processes, the presence of Ce^{3+} ions in proximity to Er^{3+} ions facilitated accumulating more electrons on $^4I_{13/2}$ (Er^{3+}) states at the cost of depopulating the $^4I_{11/2}$ (Er^{3+}) states via an energy cross-relaxation process. As a result, the UCL pathways were suppressed, while the efficiency of the radiative transition between $^4I_{13/2}$ (Er^{3+}) and $^4I_{15/2}$ (Er^{3+}) was enhanced. To verify the rationality of the proposed energy transfer processes, fluorescence decay curves associated with $^4S_{3/2}$ (Er^{3+}) → $^4I_{15/2}$ (Er^{3+}) and $^4F_{9/2}$ (Er^{3+}) → $^4I_{15/2}$ (Er^{3+}) transitions were plotted using TCSPC, as shown in Figure S4 (Supporting Information). Each decay curve on a semi-logarithmic scale was fitted by a single exponential equation. Regarding the $^4S_{3/2}(Er^{3+})$ → $^4I_{15/2}(Er^{3+})$ transition, an incremental introduction of Ce^{3+} ions from 0% to 15% resulted in a progressive reduction in fluorescence lifetime, attributed to an increased non-radiative decay rate induced from energy cross-relaxation between Ce^{3+} ions ($^2F_{5/2}$ → $^2F_{7/2}$ transition) and Er^{3+} ions ($^4S_{3/2}$ → $^4F_{9/2}$, $^4F_{9/2}$ → $^4I_{9/2}$, $^4I_{9/2}$ → $^4I_{11/2}$, and $^4I_{9/2}$ → $^4I_{13/2}$ transitions). A similar phenomenon of shortened lifetimes was observed for the $^4F_{9/2}(Er^{3+})$ → $^4I_{15/2}(Er^{3+})$ transition, however, the quenched UCL signals from nanoparticles doped with 6% or more Ce^{3+} ions were not detectable.

FTIR analysis was employed to investigate the ligands coordinated on the surface of nanoparticles, and the findings are depicted in **Figure** 3a. The characteristic peaks at 1558 and 1416 cm^{-1} indicate the asymmetric and symmetric stretching of carbonyl bonds, respectively, while the peaks at 2925 and 2851 cm^{-1} represent the vibrational stretching of methylene groups. The spectra of OA-DCNPs and PAA-DCNPs exhibited similarity, as both OA and PAA contain substantial amounts of carbonyl and methylene groups. Conversely, these characteristic peaks were absent in the spectrum of LF-DCNPs. A broad peak at 3350 cm^{-1} was assigned to the stretching vibrations of hydroxides, probably due to residual moisture present in the measured sample. Following the removal of oleate ligands through treatment with HCl, the resulting LF-DCNPs acquired a positive charge, owing to the exposure of trivalent lanthanide ions (Figure 3c). Subsequent grafting of PAA onto LF-DCNPs resulted in the acquisition of a negative surface charge, attributed to the deprotonation of carboxyl groups in the presence of hydroxides.

The morphological characterization of the film samples at various stages of nanofabrication was conducted through SEM. These characterizations are presented in **Figures** 4a–d and S5

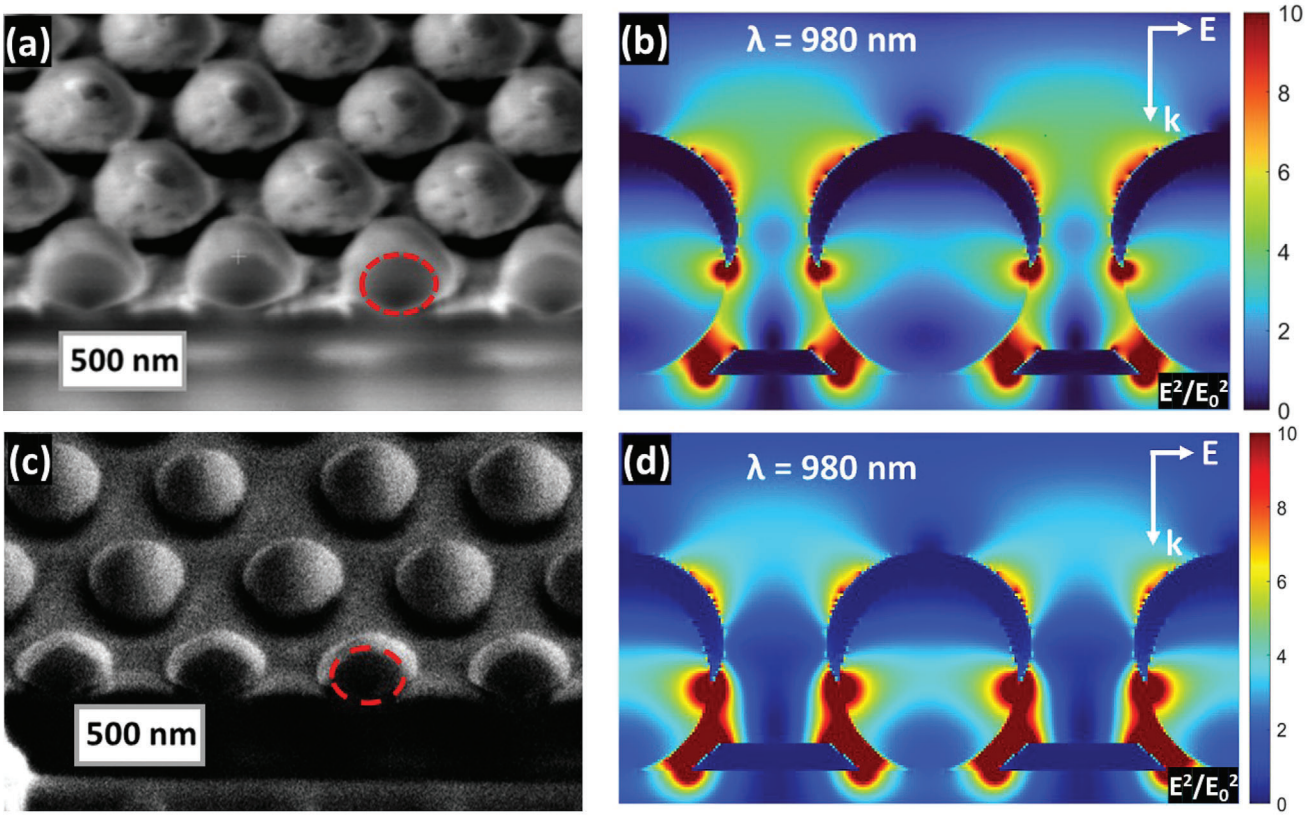

Figure 7. a,c) Cross-sectional view of (a) Ag-HCNA(50), and (c) Ag-HCNA(60); b,d) the corresponsive Local E-field enhancement calculated by 3D-FDTD modeling, using linear polarized 980 nm excitation beam source. The red dashed circle in (a) and (c) shows the area of the polystyrene sphere.

(Supporting Information). Notably, the closely packed PS sphere film, which had undergone 50 s of etching, resulted in the formation of Ag hole-cap coupled nanoarrays Ag-HCNA (50). Ag-HCNA exhibited outstanding structural periodicity and uniformity over a large area (Figure 4c,d). After a 50 s etching process, the average diameter of individual PS spheres was reduced to ≈420 nm, while the pitch size (distance from centre to centre between two adjacent spheres) was unchanged. Subsequent deposition of an Ag layer resulted in the individual Ag hemisphere caps with an average diameter of ≈465 nm, while the average separation distance between two adjacent caps was measured at ≈146 nm. A prolonged exposure to RIE, from 50 to 60 s resulted in a further reduction of PS size to ≈340 nm, reducing the gap size between an isolated Ag hemisphere caps and the hole layer. The prolonged RIE treatment resulted in an increased separation distance between adjacent Ag hemisphere caps, also contributing to a noticeable disruption in the order and regularity of the periodic array. This disruption is reflected in the larger statistical error bars associated with each structural parameter of Ag-HCNA (60), as shown in Table S1 (Supporting Information). The deposition thickness of the Ag layer and surface topographies of both types of Ag-HCNA films were confirmed using AFM, as depicted in Figure 4e,f and Figure S6 (Supporting Information). This analysis unveiled an excellent degree of periodicity of Ag-HCNA. All samples exhibit uniform heights across the measured regions. These findings are in line with the observations obtained from the SEM.

PAA-DCNPs can be effectively conjugated to the PEGylated Ag-HCNA film through the formation of amide bonds, as illustrated in **Figure** 5a. The thiol groups in the linear heterobifunctional SH-PEG-NH_2 polymeric layer exhibited a strong affinity toward the Ag-HCNA film, while the amine groups on the other end served as anchoring sites for the carboxyl groups from PAA-DCNPs. The successful grafting of the SH-PEG-NH_2 brush layer was confirmed by FTIR (Figure 5b, blue spectrum), showing characteristic peaks at 1184, 3008, and 3660 cm^{-1} representing the vibrational stretching of carbon—oxygen, hydroxide, and amine bonds, respectively. Furthermore, the decrease in water contact angle from 59.5° to 39.5° (Figure 5b, inset) indicates increased hydrophilicity of the Ag-HCNA surface after the PEGylation process.

Figure 5c shows that the DCNPs exhibited a random distribution on the Ag hemisphere caps, as well as in the gaps between adjacent spheres. Notably, DCNPs can be firmly immobilized onto the substrate due to the robust peptide bonds, even after undergoing multiple rounds of washing steps.

As shown in Figure 5d, it is evident that the pristine Ag-HCNA film exhibited multiple transmission peaks and dips across the visible and NIR regions. These distinctive spectral features were attributed to the quadra-pole plasmonic modes arising from the structural elements, including the holes, caps, and their coupled features on the Ag-HCNA substrate. Additionally, upon immobilization of DCNPs onto the Ag-HCNA surfaces, the periodicity of both Ag-HCNA types remained largely unchanged (Figure 5c and

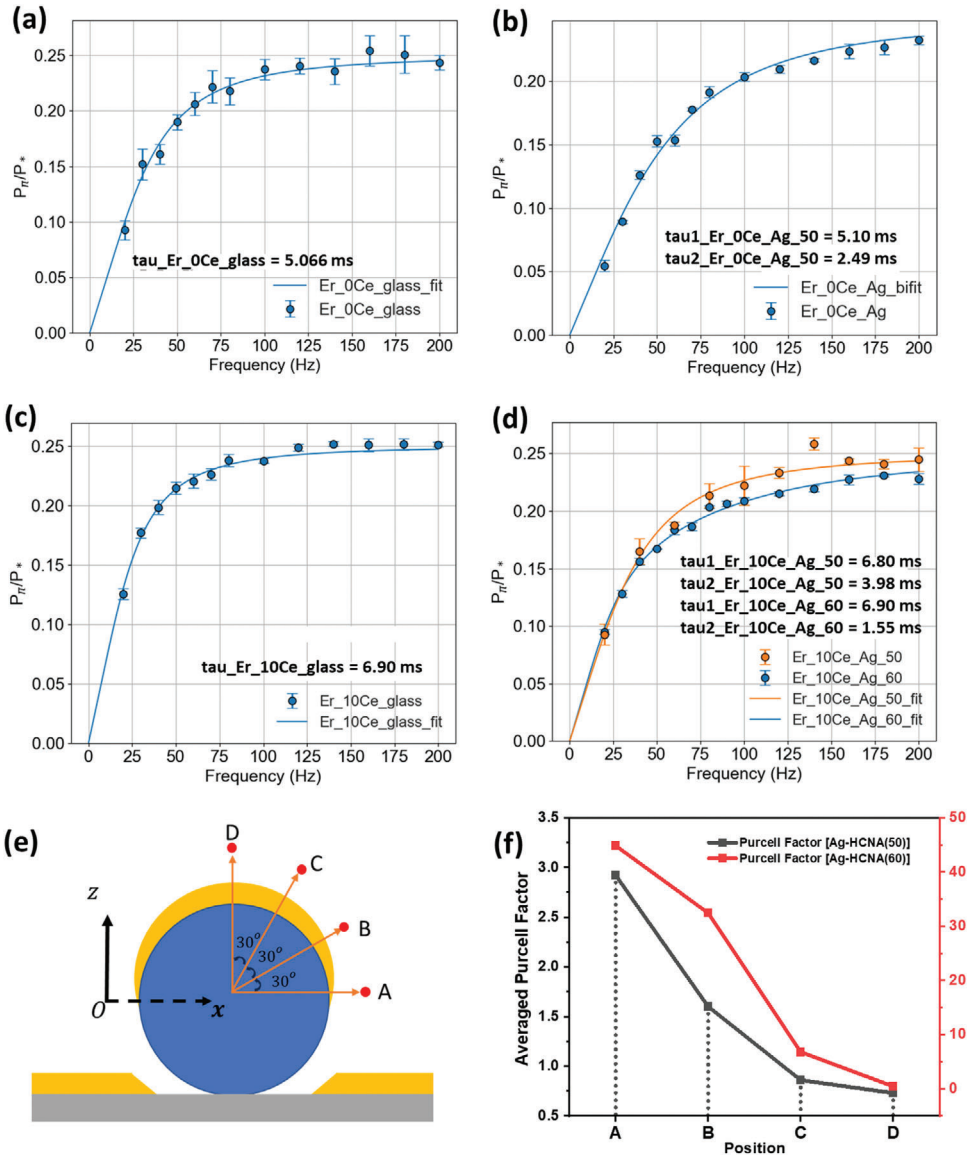

Figure 8. Lifetime measurements at 980 nm excitation of Er3+ induced NIR-II DCL emission at 1525 nm, and the simulated Purcell factor of DCL at 1525 nm. a) 0% Ce^{3+} doped DCNPs on glass and the corresponding mono-exponential fit curve, b) 0% Ce^{3+} doped DCNPs immobilized Ag-HCNA substrate, and the bi-exponential fit curve. c) 10% Ce^{3+} doped DCNPs on glass and the corresponding mono-exponential fit curve. d) 10% Ce^{3+} doped DCNPs immobilized Ag-HCNA(50) and Ag-HCNA(60) substrates and the bi-exponential fit curve. e, f) Purcell factor simulations for both types of Ag-HCNA structures with varying geometries. Ag-HCNA(50) film exhibited a larger Ag hemisphere cap of ≈465 nm in diameter and a reduced separation distance between adjacent Ag hemisphere caps of ≈146 nm. In contrast, the Ag-HCNA(60) film featured a smaller Ag hemisphere cap of ≈384 nm in diameter and a larger separation distance of ≈204 nm. e) schematic illustrations Purcell factor modeling configuration. f) the average Purcell factors versus positions.

Figure S7, Supporting Information). Hence, it was deduced that the observed slight redshift in the transmission peaks for both substrates was mainly attributed to the heightened refractive index introduced by the DCNP layer. Through precise control of oxygen etching time and the thickness of the Ag layer, the prominent transmission peak and dip at ≈980 nm can be finely tuned to closely match the absorption band of the sensitizer ions Yb^{3+} present within DCNPs (Figure S8, Supporting Information).

To investigate the plasmonic effect of Ag-HCNA on the enhancement of NIR-II DCL signals, two varieties of DCNPs were manufactured, doped with 0% and 10% Ce^{3+} ions (labeled as DCNPs (0% Ce) and DCNPs (10% Ce), respectively). These DNCPs were employed in conjunction with Ag-HCNA films and were excited by a 980 nm laser. As depicted in Figure 5e, it was evident that the emission intensity of Er^{3+} induced NIR-II DCL from DCNPs (10% Ce) on glass was ≈6 times higher than that from DCNPs (0% Ce) on glass, corroborating the observations in Figure 2b. Notably, when either DCNPs (0% Ce) or DCNPs (10% Ce) were coupled to Ag-HCNA(50), an enhancement of up to 10-fold was observed compared to their counterparts on glass.

Further, a substantial enhancement of up to 25-fold was observed when DCNPs (10% Ce) were immobilized onto an Ag-HCNA (60) film. Furthermore, a synergistic enhancement effect was achieved by doping 10% of Ce^{3+} ions into co-doped $NaYF_4$:Yb^{3+}, Er^{3+} DCNPs and coupling them with Ag-HCNA (60), resulting in an impressive 120-fold luminescence enhancement at 1525 nm (Figure S9, Supporting Information). This represents an effective strategy for overcoming the low efficiency of DCL signals typically associated with conventional $NaYF_4$:Yb^{3+}, Er^{3+} DCNPs.

Both Ag-HCNA coupled and pristine DCNPs exhibited outstanding photostability even after prolonged exposure to a laser source, as shown in Figure 5f. This can be attributed to the shielding effect of the filled 5s and 5p sub-orbitals, which localize the energy transitions of lanthanide ions within the 4f inner orbitals and render them minimally influenced by the surrounding environment. Given the substantial enhancement in DCL signals in the NIR-II region and the exceptional photostability exhibited, the integration of Ag-HCNA with DCNPs represents an ideal plasmonic platform for advancing the field of next-generation DCNPs' applications in the NIR-II window.

Figure 6a shows the emission intensities of DCNPs (10% Ce) on glass, Ag-HCNA (50), and Ag-HCNA (60) substrates, as a function of excitation power. The experimental data were fitted according to:

$$I = I_{\infty} \times P/\left(P + P_{sat}\right) \tag{1}$$

Where P and I represent excitation power density and the observed emission intensity, respectively. P_{sat} and I_{∞} denote the excitation power density and the emission rate at saturation.[51] The fitting indicates $I_{\infty} \approx 1.1 \times 10^7$ counts s^{-1} at $P_{Sat} \approx 70$ kW cm^{-2} for pristine DCNPs on glass. In comparison, the value of I_{∞} DCNPs on Ag-HCNA(50) and Ag-HCNA(60) substrates were increased to $\approx 2.2 \times 10^7$ counts s^{-1} and 3.5×10^7 counts s^{-1}, respectively. $P_{Sat}$for these two substrates were 56and 62 kW cm^{-2}, respectively. The altered saturation behavior observed in DCNPs onto Ag-HCNA indicated a similarity to findings in a prior study where a lower saturation power for Er^{3+} induced UCL was observed in DCNPs coupled to plasmonic gold nanorod arrays.[26] Figure 6b depicts the Log-Log plots of the excitation power-dependent NIR-II DCL intensity of DCNPs (10% Ce), both on glass and immobilized on Ag-HCNA samples, at a low excitation regime. It is worth highlighting that both plasmonic-affected and reference DCNPs exhibited a nearly linear dependence on the excitation power density, which is consistent with our previously reported work.[43]

In general, two primary categories of plasmonic enhancement modes, namely excitation enhancement and emission rate enhancement are considered when DCNPs are positioned near metallic nanostructures. For excitation enhancement, the large localized electric field induced at the excitation wavelength boosts the absorption cross-section and accelerates the excitation rate of Yb^{3+} within DCNPs. The accelerated rate of excitation shows a direct proportionality to the enhancement in local electric field intensity:

$$\frac{r}{r_0} \propto \frac{E^2}{E_0^2} \tag{2}$$

Where r_0 and r denote the intrinsic and plasmonic-enhanced excitation rate of DCNPs, respectively. $E_0$is the magnitude of the incident electric field and E being the enhanced localized field.

Figure 7 shows that when a 980 nm linear polarized beam is applied, the intensity of local electric fields exhibited variation at different positions along Ag-HCNA. A maximum of up to 10-fold excitation rate enhancement of Yb^{3+} was estimated when DCNPs are immobilized at the edges of Ag-HCNA. Due to the "one photon" luminescence process, the emission intensity of Er^{3+} induced NIR-II DCL performed a linear dependence on the intensity of the local electric field that DCNPs experienced.

If no other factors were at play, the intensity of Er^{3+} induced NIR-II DCL can also be enhanced by 10-fold. However, the competitive radiative and non-radiative decay rate of Yb^{3+} may also be improved by the plasmonic characteristics of Ag-HCNA, leading to the faster depopulation of $^2F_{5/2}$ (Yb^{3+}) and suppressing DCL processes.

For the emission rate enhancement, the radiative decay rate of Er^{3+} emitting 1525 nm photons can be accelerated by the Purcell effect through plasmonic confinement, and the quantum yield of luminescence can be improved.[52] For a comprehensive understanding, we measured the fluorescence lifetimes at 1525 nm from DCNPs both on glass and on Ag-HCNA. **Figure 8**a,c show that DCNPs doped with 10% of Ce^{3+} possessed an intrinsically longer lifetime of ≈6.9 ms compared to those without Ce^{3+} dopants (≈5.1 ms), attributed to that the presence of Ce^{3+} boosted the possibility of $^4I_{13/2}$ (Er^{3+}) state population. Figure 8b,d show that the decay curves for both two types of DCNPs immobilized onto Ag-HCNA can be fitted by two distinct emitter lifetimes, equivalent to a bi-exponential fit: the longer lifetime is attributed to uncoupled Er^{3+} within DCNPs and the shorter one to the plasmonic-coupled Er^{3+}. In Figure 8b, ≈70% of the emitted photons with a lifetime reduced to ≈2.49 ms originated from plasmonic-enhanced DCNPs, while the remaining ≈30% came from DCNPs (0% Ce) uncoupled by Ag-HCNA. Figure 8d also revealed a similar trend, with ≈72.5% of emitted photons exhibiting a decreased lifetime (from 6.8 to 3.98 ms), likely stemming from DCNPs (10% Ce) coupled to Ag-HCNAs, and the remaining ≈27.5% matching the lifetime of DCNPs (10% Ce) on glass. In the case of DCNPs (10% Ce) on Ag-HCNA(60), ≈33% of emitted photons showed a significantly reduced lifetime of ≈1.55 ms.

Previous studies show that both radiative and non-radiative decay rates of fluorophores can be increased when coupled with metallic nanostructures.[53,54] The former directly contributes to the enhancement of fluorescence. Nevertheless, a simultaneous increase in the non-radiative decay rate of the emitters contributes to fluorescence quenching. Quenching becomes pronounced when the emitters are in close contact with the metallic surface.[20,55] In this study, the heterobifunctional SH-PEG-NH_2 polymeric layer plays a crucial role in effectively separating DCNPs from the Ag surface. By providing such a dielectric spacer layer over 5 nm,[44] the non-radiative decay rate can be largely mitigated, resulting in the net NIR-II DCL enhancement rather than quenching.

From Figure 5c and Figure S7 (Supporting Information), the distribution of the immobilized DCNPs on the Ag-HCNA surface was observed to be stochastic, resulting in the formation of a sub-monolayer that adhered to both the apex and base positions of the Ag-HCNA. As such, we assumed that the sensitizer Yb^{3+}

ions within individual DCNPs experienced excitation enhancement due to the localized electric field distribution above the Ag surface.

As depicted in the local E-field diagram in Figure S10 (Supporting Information), Ag-HCNA exhibited a localized electric field with varying degrees of enhanced intensity under the excitation of 980 nm. For instance, assuming that the whole surface of Ag-HCNA(50) is evenly covered by closely packed DCNPs (10% Ce) with an average diameter of 40 nm, only ≈20% of the total DCNPs could experience a substantial 10-fold enhancement in electric field intensity, while ≈60% of DCNPs experience a local E-field intensity enhancement between 2 and 6. The remaining 20% of DCNPs experience negligible field enhancement. We can further simplify this model by considering a monolayer of DCNPs (0% Ce) with an average diameter of 26 nm. In this scenario, ≈25% of DCNPs are positioned within electric field "hot spots," contributing to the maximum electric field enhancement for the coupled DCNPs, while the remaining DCNPs experience negligible electric field enhancement.

For DCNPs (10% Ce) on both Ag-HCNA (50) and Ag-HCNA(60), the estimated percentage of DCNPs within "hot spots" is ≈20%. As such, a valid estimation of the quantum yield η'/η in a real scenario is expected to be lower than that calculated using the assumed condition because the low E-field enhancement regions were not considered. With the known parameters, including Enh_{total}, Γ_{total}, and Γ'_{total}, the enhanced quantum yields by comparing plasmonic-coupled DCNPs and origin DCNPs were estimated to be $\eta'/\eta \leq 1.5$ for DCNPs (10% Ce) on Ag-HCNA(50), $\eta'/\eta \leq 1.2$ for DCNPs (0% Ce^{3+}) on Ag-HCNA(50), and $\eta'/\eta \leq 2.7$ for DCNPs (10% Ce) on Ag-HCNA(60). These results indicate that the observed NIR-II DCL enhancement was dominated by excitation enhancement. The lifetime results also align with the observations shown in Figure 6a, where the saturation excitation power of DCNPs on Ag-HCNA is slightly lower than the original DCNPs. This can be explained by the fact that the increased population density of $^2F_{5/2}$ state (Yb^{3+}) by field enhancement induced by Ag-HCNA is higher than the increased decay rate at 1525 nm

Figure 8 e,f show the simulated Purcell factor of emitters positioned close to the surface of both types of Ag-HCNA structures. Notably, a higher Purcell factor was observed near the edge of the Ag hemisphere cap, with the Ag-HCNA(60) structure exhibiting a significantly larger Purcell factor compared to Ag-HCNA (50). Interestingly, the averaged Purcell factors for various positions are larger for Ag-HCNA(60) than Ag-HCNA(50). This result highly aligned with the radiative decay rate enhancement of DCNPs (10% Ce) on both Ag-HCNA types, as shown in Table S2 (Supporting Information). In practice, the measured Purcell factor represented a value averaged over the emitters distributed on all surfaces of the structures, which is within the interval of simulated values. In future investigations, achieving precise control over emitter distribution and their relative positioning with plasmonic antennas becomes a crucial avenue for fully harnessing the cavity effect to enhance luminescence.

4. Conclusion

This study demonstrates a novel strategy to enhance DCNPs' emission in the NIR-II region by synergistically combining Ce^{3+} doping and plasmonic coupling. To enhance the NIR-II emission of DCNPs, the conventional Yb^{3+}/Er^{3+} co-doped DCNPs were further modified by incorporating Ce^{3+} ions, promoting $^4I_{13/2}$ (Er^3) → $^4I_{15/2}$ (Er^3) transitions, with a peak emission in the NIR-II at 1525 nm. The plasmonic Ag-HCNA film featuring multi-band extinction characteristics was successfully fabricated using a simple yet robust colloidal lithography technique.

A 25-fold luminescent enhancement in NIR-II was achieved when a sub-monolayer of Ce^{3+} doped DCNPs was affixed to Ag-HCNA through amide bonds. Significantly, combining a 10% Ce^{3+} doping with NaYF4:Yb^{3+}, Er^{3+} DCNPs and coupling them with Ag-HCNA (60) film resulted in a 120-fold enhancement of downconversion luminescence in NIR-II window. These results outperformed dramatically conventional $NaYF_4$:Yb^{3+}, Er^{3+} co-doped DCNPs on glass substrates. Our findings were further substantiated by 3D-FDTD simulations and lifetime measurements at 1525 nm, highlighting that the predominant factor contributing to the observed DCL enhancement was the local electric field enhancement, particularly at the coupled region between the Ag hemisphere and nanohole. In contrast, the contribution of emission rate enhancement remained relatively limited.

In summary, this work introduced a novel strategy to amplify weak NIR-II signals using both doping and plasmonic technology, providing significant opportunities for future DCNPs' applications in the NIR-II window.

Supporting Information

Supporting Information is available from the Wiley Online Library or from the author.

Acknowledgements

This work was supported by Imperial College London, the President's Excellence Fund for Frontier Research (awarded to F.X. from 2021 to 2024). S.A.M., R.O., and F.X. acknowledge EPSRC program grant EP/W017075/1. The authors acknowledge the use of characterization facilities within the Harvey Flower Electron Microscopy Suite at the Department of Materials, Imperial College London. The authors acknowledge support from the Henry Royce Institute made through EPSRC grant EP/R00661X/1.

Conflict of Interest

The authors declare no conflict of interest.

Data Availability Statement

The data that support the findings of this study are available from the corresponding author upon reasonable request.

Keywords

lanthanide downconversion nanoparticles (DCNPs), light-matter interaction, Near Infrared Second (NIR-II), plasmonics

Received: March 9, 2024
Revised: July 16, 2024
Published online:

[1] A. Escudero, A. Becerro, C. Carrillo-Carrión, N. O. Núñez, M. V. Zyuzin, M. Laguna, D. González-Mancebo, M. Ocaña, W. J. Parak, *Nanophotonics* **2017**, *6*, 881.
[2] T. Jia, G. C. Chen, *Chem. Rev.* **2022**, *471*, 214724.
[3] L. Sun, Y. Huang, C. Ji, C. A. Grimes, Q. Cai, *Sens. Actuators, B* **2023**, *384*, 133669.
[4] P. Wang, Y. Fan, L. Lu, L. Liu, L. Fan, M. Zhao, Y. Xie, C. Xu, F. Zhang, *Nat. Commun.* **2018**, *9*, 2898.
[5] T. Yang, J. Qin, J. Zhang, L. Guo, M. Yang, X. Wu, M. You, H. Peng, *Chemosensors* **2022**, *10*, 206.
[6] Y. Yang, D. Tu, Y. Zhang, P. Zhang, X. Chen, *iScience* **2021**, *24*, 102062.
[7] Z. Yu, C. Eich, L. J. Cruz, *Front. Chem.* **2020**, *8*, 496.
[8] Y. Zhong, H. Dai, *Nano Res.* **2020**, *13*, 1281.
[9] W. Liang, S. He, S. Wu, *Adv. NanoBiomed Res* **2022**, *2*, 2200087.
[10] G. Hong, A. L. Antaris, H. Dai, *Nat. Photonics* **2014**, *8*, 723.
[11] Z. Feng, T. Tang, T. Wu, X. Yu, Y. Zhang, M. Wang, J. Zheng, Y. Ying, S. Chen, J. Zhou, *Light: Sci. Appl.* **2021**, *10*, 197.
[12] S. V. Eliseeva, J.-C. G. Bünzli, *Chem. Soc. Rev.* **2010**, *39*, 189.
[13] S. Han, R. Deng, X. Xie, X. Liu, *Angew. Chem., Int. Ed.* **2014**, *53*, 11702.
[14] C. Cheng, Y. Xu, G. De, J. Wang, W. Wu, Y. Tian, S. Wang, *CrystEngComm* **2020**, *22*, 6330.
[15] Y. Li, C. Liu, P. Zhang, J. Huang, H. Ning, P. Xiao, Y. Hou, L. Jing, M. Gao, *Front. Chem.* **2020**, *8*, 832.
[16] L. Wang, W. Yang, L. Li, S. Hu, M. Yuan, Z. Yang, K. Han, H. Wang, X. Xu, *ACS Omega* **2022**, *7*, 27230.
[17] K. Nagamatsu, S. Nagaoka, M. Higashihata, N. J. Vasa, Z. Meng, S. Buddhudu, T. Okada, Y. Kubota, N. Nishimura, T. Teshima, *Opt. Mater.* **2004**, *27*, 337.
[18] Y. Zhong, Z. Ma, S. Zhu, J. Yue, M. Zhang, A. L. Antaris, J. Yuan, R. Cui, H. Wan, Y. Zhou, W. Wang, N. F. Huang, J. Luo, Z. Hu, H. Dai, *Nat. Commun.* **2017**, *8*, 737.
[19] S. M. Fothergill, C. Joyce, F. Xie, *Nanoscale* **2018**, *10*, 20914.
[20] I. G. Theodorou, Z. A. R. Jawad, Q. Jiang, E. O. Aboagye, A. E. Porter, M. P. Ryan, F. Xie, *Chem. Mater.* **2017**, *29*, 6916.
[21] I. G. Theodorou, Z. A. R. Jawad, H. Qin, E. O. Aboagye, A. E. Porter, M. P. Ryan, F. Xie, *Nanoscale* **2016**, *8*, 12869.
[22] L. Trotsiuk, A. Muravitskaya, O. Kulakovich, D. Guzatov, A. Ramanenka, Y. Kelestemur, H. V. Demir, S. Gaponenko, *Nanotechnology* **2019**, *31*, 105201.
[23] Y. Yang, A. Dev, I. Sychugov, C. Hägglund, S.-L. Zhang, *J. Phys. Chem. Lett.* **2023**, *14*, 2339.
[24] A. Chu, H. He, Z. Yin, R. Peng, H. Yang, X. Gao, D. Luo, R. Chen, G. Xing, Y. J. Liu, *ACS Appl. Mater. Interfaces* **2019**, *12*, 1292.
[25] J. He, W. Zheng, F. Ligmajer, C.-F. Chan, Z. Bao, K.-L. Wong, X. Chen, J. Hao, J. Dai, S.-F. Yu, *Light: Sci. Appl.* **2017**, *6*, 16217.
[26] Z. Yin, D. Zhou, W. Xu, S. Cui, X. Chen, H. Wang, S. Xu, H. Song, *ACS Appl. Mater. Interfaces* **2016**, *8*, 11667.
[27] M. Bauch, K. Toma, M. Toma, Q. Zhang, J. Dostalek, *Plasmonics* **2014**, *9*, 781.
[28] D. M. Wu, A. García-Etxarri, A. Salleo, J. A. Dionne, *J. Phys. Chem. Lett.* **2014**, *5*, 4020.
[29] J. Malicka, I. Gryczynski, J. R. Lakowicz, *J. Biomed. Opt.* **2003**, *8*, 472.
[30] F. Xie, J. S. Pang, A. Centeno, M. P. Ryan, D. J. Riley, N. M. Alford, *Nano Res.* **2013**, *6*, 496.
[31] J. Xu, W. Morton, D. Jones, T. A. Tabish, M. P. Ryan, F. Xie, *Appl. Phys. Rev.* **2022**, *9*, 031303.
[32] Z. A. Jawad, L. Li, Y. Hou, T. Yang, L. Wang, Z. Chen, et al., *Sci. Rep.* **2017**, *7*, 14309.
[33] K. Aslan, J. R. Lakowicz, C. D. Geddes, *Curr. Opin. Biotechnol.* **2005**, *16*, 55.
[34] R. Zhang, Z. Jin, Z. Tian, Y. Liu, Z. Lu, Y. Cui, *RSC Adv.* **2021**, *11*, 7723.
[35] L. Zhou, F. Ding, H. Chen, W. Ding, W. Zhang, S. Y. Chou, *Anal. Chem.* **2012**, *84*, 4489.
[36] M. Supianto, H. J. Lee, *Bull. Korean Chem. Soc.* **2022**, *43*, 1.
[37] Y. Li, J. Ke, Q. Liu, W. Yuan, Q. Su, M. Kong, N. Wu, W. Feng, C. Huang, F. Li, *Sens. Actuators, B* **2021**, *345*, 130380.
[38] R. Chen, X. Zhou, Y. Wu, Q. Liu, Q. Liu, J. Huang, F. Li, *Sens. Actuators, B* **2021**, *328*, 129050.
[39] L. Ao, T. Liao, L. Huang, S. Lin, K. Xu, J. Ma, S. Qiu, X. Wang, Q. Zhang, *Chem. Eng. J.* **2022**, *436*, 135204.
[40] F. Wang, R. Deng, X. Liu, *Nat. Protoc.* **2014**, *9*, 1634.
[41] N. Bogdan, F. Vetrone, G. A. Ozin, J. A. Capobianco, *Nano Lett.* **2011**, *11*, 835.
[42] W. Kong, T. Sun, B. Chen, X. Chen, F. Ai, X. Zhu, M. Li, W. Zhang, G. Zhu, F. Wang, *Inorg. Chem.* **2017**, *56*, 872.
[43] J. Xu, M. Fu, C. Ji, A. Centeno, D. K. Kim, K. Evers, S. E. M. Heutz, R. Oulton, M. P. Ryan, F. Xie, *Adv. Opt. Mater.* **2023**, *11*, 2300477.
[44] I. G. Theodorou, Q. Jiang, L. Malms, X. Xie, R. C. Coombes, E. O. Aboagye, A. E. Porter, M. P. Ryan, F. Xie, *Nanoscale* **2018**, *10*, 15854.
[45] H. Qin, D. Wu, J. Sathian, X. Xie, M. P. Ryan, F. Xie, *Sci. Rep.* **2018**, *8*, 12683.
[46] N. A. Güsken, M. Fu, M. Zapf, M. P. Nielsen, P. Dichtl, R. Röder, A. S. Clark, S. A. Maier, C. Ronning, R. F. Oulton, *Nat. Commun.* **2023**, *14*, 2719.
[47] A. F. Oskooi, D. Roundy, M. Ibanescu, P. Bermel, J. D. Joannopoulos, S. G. Johnson, *Comput. Phys. Commun.* **2010**, *181*, 687.
[48] A. D. Rakić, A. B. Djurišic, J. M. Elazar, M. L. Majewski, *Appl. Opt.* **1998**, *37*, 5271.
[49] A. Centeno, In *Asia-Pacific Conference on Applied Electromagnetics* **2003**, 128.
[50] X. Lei, R. Li, D. Tu, X. Shang, Y. Liu, W. You, C. Sun, F. Zhang, X. Chen, *Chem. Sci.* **2018**, *9*, 4682.
[51] T. T. Tran, K. Bray, M. J. Ford, M. Toth, I. Aharonovich, *Nat. Nanotechnol.* **2016**, *11*, 37.
[52] M. Fu, M. P. D. P. Mota, X. Xiao, A. Jacassi, N. A. Güsken, Y. Chen, H. Xiao, Y. Li, A. Riaz, S. A. Maier, R. F. Oulton, *Nat. Nanotechnol.* **2022**, *17*, 1251.
[53] R. Carminati, J. J. Greffet, C. Henkel, *Opt. Commun.* **2006**, *261*, 368.
[54] N. Cade, M. M. Alkaisi, Y. Zhang, F. Zhou, H. Gao, P. Bartlett, *Nanotechnology* **2009**, *20*, 285201.
[55] P. Bharadwaj, L. Novotny, *Opt. Express* **2007**, *15*, 14266.